PNAS
RESEARCH ARTICLE | CELL BIOLOGY

# Cotranslational molecular condensation of cochaperones and assembly factors facilitates axonemal dynein biogenesis

Yuanyuan Li[a], Wenyan Xu[a], Yubao Cheng[a], Lydia Djenoune[b], Chuzhi Zhuang[a], Andrew Lee Cox[a], Clemente J. Britto[c], Shiaulou Yuan[b], Siyuan Wang[a,d], and Zhaoxia Sun[a,1]

Affiliations are included on p. 10.

Edited by Steven L. Brody, Washington University in St. Louis School of Medicine, St. Louis, MO; received February 14, 2024; accepted October 10, 2024 by Editorial Board Member Yale E. Goldman

**Axonemal dynein, the macromolecular machine that powers ciliary motility, assembles in the cytosol with the help of dynein axonemal assembly factors (DNAAFs). These DNAAFs localize in cytosolic foci thought to form via liquid–liquid phase separation. However, the functional significance of DNAAF foci formation and how the production and assembly of multiple components are so efficiently coordinated, at such enormous scale, remain unclear. Here, we unveil an axonemal dynein production and assembly hub enriched with translating heavy chains (HCs) and DNAAFs. We show that mRNAs encoding interacting HCs of outer dynein arms colocalize in cytosolic foci, along with nascent HCs. The formation of these mRNA foci and their colocalization relies on HC translation. We observe that a previously identified DNAAF assembly, containing the DNAAF Lrrc6 and cochaperones Ruvbl1 and Ruvbl2, colocalizes with these HC foci, and is also dependent on HC translation. We additionally show that Ruvbl1 is required for the recruitment of Lrrc6 into the HC foci and that both proteins function cotranslationally. We propose that these DNAAF foci are anchored by stable interactions between translating HCs, ribosomes, and encoding mRNAs, followed by cotranslational molecular condensation of cochaperones and assembly factors, providing a potential mechanism that coordinates HC translation, folding, and assembly at scale.**

cilia | dynein axonemal assembly factors | co-translational assembly | primary ciliary dyskinesia | Ruvbl1/Ruvbl2

Motile cilia are essential cellular appendages distributed in multiple organs/tissues to drive cell movement or extracellular fluid flow and are fundamental to an array of physiological processes. For example, motile cilia contribute significantly to establishing left–right asymmetry during embryonic development, propel sperm movement, and function in the respiratory epithelium to orchestrate the rhythmic, high-frequency beating [over 10 Hz (beats/s)] that drives airway clearance—a frontline defense mechanism against pathogens (1).

The motile cilium is powered by inner and outer dynein arms (IDAs and ODAs), subunits of which are folded and preassembled in the cytosol before being delivered into the cilium (2, 3). Axonemal dyneins are the motor of dynein arms and they are composed of proteins with varying sizes, ranging from small light chains (LCs; <200 amino acids) to large heavy chains (HCs; ~4,500 residues). Large numbers of these proteins need to be synthesized during motile ciliogenesis (4, 5). Our understanding of the molecular mechanisms that ensure the efficient and accurate biogenesis of axonemal dynein at scale in the crowded cytosol remains limited.

The leading hypothesis suggests that a group of dynein axonemal assembly factors (DNAAFs) facilitate axonemal dynein assembly (6–14) by concentrating into droplet-shaped foci (15–17) via liquid–liquid phase separation (LLPS), a phenomenon through which components condense from a liquid and segregate to form another membraneless liquid compartment via a plethora of weak interactions (18). However, in vivo evidence supporting the functional significance of LLPS in axonemal dynein assembly is limited. In addition, the current model does not address how intercomponent interactions occur efficiently and accurately in the crowded cytosol at scale, how aggregate formation is prevented, given the very high local concentration of translating HCs, and how the production of multiple dynein arm components of different sizes is coordinated.

We previously isolated a group of mutants with almost identical cilia-associated phenotypes in zebrafish via a large-scale insertional mutagenesis screen (19). Using these mutants, we subsequently showed that Ruvbl1/Pontin and Ruvbl2/Reptin (R2) function as cochaperones for dynein arm assembly, and observed that Ruvbl1, Ruvbl2, and the

## Significance

Axonemal dynein, the macromolecular machine that powers ciliary motility, is produced in large quantities in the crowded cytosol. However, how the production and assembly of multiple components are efficiently coordinated at scale remains unclear. Here, we unveil a cotranslational molecular condensation mechanism. We show that large stable scaffolds consisting of translating heavy chains, ribosomes, and encoding mRNAs drive molecular condensation of cochaperones and assembly factors. We identify cotranslational assembly as an early step of axonemal dynein biogenesis and placed the dynein axonemal assembly factor Lrrc6 and the cochaperones Ruvbl1 and Ruvbl2 in this step. Our model provides a potential mechanism for coordinating heavy chain translation, folding, and assembly at scale.

Competing interest statement: S.W. is a shareholder and consultant of Translura, Inc. The remaining authors declare no competing interests.

This article is a PNAS Direct Submission. S.L.B. is a guest editor invited by the Editorial Board.

[1] To whom correspondence may be addressed. Email: zhaoxia.sun@yale.edu.

This article contains supporting information online at https://www.pnas.org/lookup/suppl/doi:10.1073/pnas.2402818121/-/DCSupplemental.

DNAAF Lrrc6, form cytosolic round foci in motile ciliated cells (15, 16, 20). Here, we present a cotranslational molecular condensation mechanism that connects HC translation and DNAAF foci formation. We show that active translation of HCs leads to the formation of nascent HC-mRNA scaffolds that initiate molecular condensation of cochaperones Ruvbl1, Ruvbl2, and the DNAAF Lrrc6, and that Ruvbl1 and Lrrc6 function cotranslationally. Our findings reveal a significant role for the stable interactions between HC mRNA and translating HCs in foci-formation, offer insights into axonemal dynein biogenesis and provide a potential mechanism that ensures the folding and assembly of highly concentrated nascent HCs.

## Results

**HC mRNAs Colocalize in Cytosolic Foci Containing Translating HCs.** Considering the scale and complexity of the biogenesis of axonemal dynein motors, we hypothesized that a cotranslational mechanism could potentially coordinate the synthesis of multiple protein subunits and their organization into a functional complex in the crowded cytosol. We utilized the zebrafish pronephric duct (PND) to test this hypothesis.

In zebrafish, the PND is lined with motile cilia (21). Previous studies revealed both multiciliated and monociliated cells in the PND and suggested that both are formed by 48 h postfertilization (hpf) (21–23). To investigate the dynamic process of axonemal dynein biogenesis and maintenance, we investigated the timeline of ciliogenesis in the PND in more detail. We first visualized cilia at 36 hpf via immunostaining using the cilia marker anti-acetylated tubulin. Consistent with previous reports, ciliary signal could be seen throughout the PND but significantly stronger in a region next to the transition between the yolk ball and yolk extension, which we called the "middle" region (*SI Appendix*, Fig. S1 *A* and *B*). We then expanded this analysis to include more timepoints and the basal body marker anti-γ-tubulin. Notably, at 25 hpf, although long single cilia were detected in all regions, basal body clusters emerged in the mid-region (*SI Appendix*, Fig. S1*C*), suggesting that multiciliogenesis commences earlier and is already active at 25 hpf in the middle region. Therefore, in this study, we focused on this region unless otherwise specified (Fig. 1*A*).

We first investigated the subcellular localization patterns of mRNAs encoding ODA dynein components at 25 hpf using fluorescence in situ hybridization. The zebrafish ODA dynein consists of two HCs (β and γ-HCs), together with intermediate chains (ICs) and light chains (LCs). While mRNAs encoding IC (*dnai1.2* and *dnai2b*) and LC (*dnal1*) components formed dispersed puncta, *dnah5* and *dnah9* mRNAs, encoding a pair of interacting γ- and β-HCs, respectively, were observed in foci of varying sizes (Fig. 1*B*). In addition, *dnah5* and *dnah9* mRNA foci partially colocalized (Fig. 1*B*). The specificity of the signals was verified by their enrichment within the PND, but not in surrounding regions (*SI Appendix*, Fig. S1*D*). Pixel-based, slice-by-slice colocalization analysis on Z-stacks showed an average Pearson correlation coefficient of 0.59 between signals of *dnah5* and *dnah9* mRNA, supporting significant correlation between the localization of the two mRNAs (Fig. 1 *C* and *D* and Movie S1). In contrast, the average correlation coefficient between *dnah5* mRNA and *dnai1.2, dnai2b,* or *dnal1* mRNA was 0.08, 0.07, and 0.08, respectively, suggesting no significant correlation (Fig. 1 *C* and *D* and Movie S1). Combined, these results revealed partial but specific colocalization between *dnah5* and *dnah9* mRNA.

We then analyzed the subcellular localization of Dnah9 protein at 25 hpf by immuno-fluorescence staining combined with in situ hybridization. Dnah9 protein was found in cilia-like structures

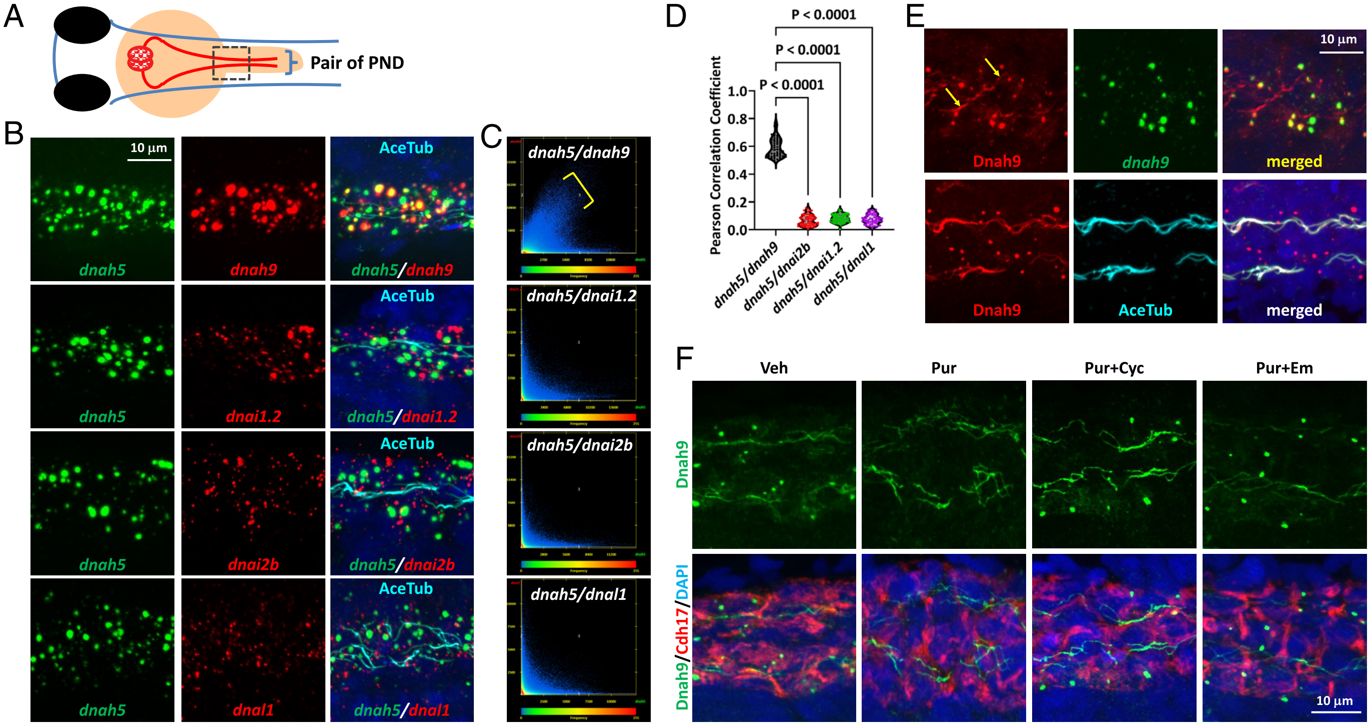

**Fig. 1.** mRNAs encoding interacting HCs partially colocalize in cytosolic foci containing translating HCs. (*A*) A diagram depicting the imaged area (boxed). (*B*) Z-projections showing localization patterns of axonemal dynein mRNAs at 25 hpf. Cilia indicated by AceTub (cyan). (*C*) Z-projections of scatter plots of pixel intensity between two mRNAs. Bracket in the *Top* panel indicates pixels showing intensity correlation in two channels. (*D*) Pearson correlation coefficient between signals of two mRNAs. Pooled from slices of three embryos per condition. (*E*) Localization of Dnah9 protein shown by Z-projections at 25 hpf. *Upper*: Dnah9 protein (red) in foci with *dnah9* mRNA (green), and cilia-like structures (arrows). *Lower*: Dnah9 (red) on cilia (AceTub, cyan) and cytoplasmic foci. (*F*) Dnah9 protein (green) foci are sensitive to puromycin treatment as shown by Z-projections. Cdh17 in red labels the PND. AceTub: anti-acetylated tubulin signal; Veh: vehicle; Pur: puromycin; Pur+Cyc: puromycin and cycloheximide; Pur+Em: puromycin and emetine.

(Fig. 1 *E*, *Upper* panels, arrow), which was verified by colabeling with the cilia marker anti-acetylated tubulin (Fig. 1 *E*, *Lower* panels). Interestingly, we additionally detected Dnah9-positive foci in the cytosol that colocalized with *dnah9* mRNA foci (Fig. 1 *E*, *Upper* panels), indicating active translation rather than storage of *dnah9* mRNA at these sites. To validate this finding, we blocked protein translation acutely using puromycin, a Tyr-tRNA mimetic that induces premature translation termination and release of nascent peptides from mRNA. Fifteen minutes after puromycin injection, Dnah9 foci in the cytosol had rapidly dissipated, while the Dnah9 signal within cilia, representing mature Dnah9 already trafficked to cilia, remained unchanged (Fig. 1*F*). Automatic segmentation followed by quantification verified a significant reduction of foci number in puromycin treated samples (*SI Appendix*, Fig. S1*E*). As controls, we coinjected puromycin together with cycloheximide or emetine, elongation inhibitors that immobilize nascent peptides on ribosomes and thus prevent the release of nascent peptides by puromycin. The results showed that in the presence of emetine or cycloheximide, puromycin failed to disrupt Dnah9 foci, supporting the specificity of this treatment (Fig. 1*F* and *SI Appendix*, Fig. S1*E*). These findings suggest that Dnah9 signal in cytosolic foci represents translating peptides.

**HC mRNA Foci Formation and Colocalization Require Active HC Translation.** Due to the sheer size of HC mRNA and the need for large numbers of HCs, it is likely that single HC mRNA molecules are decorated by multiple copies of nascent HCs during protein synthesis. Moreover, β and γ HCs interact via their N-terminal tail (24), suggesting that interactions between translating HCs would bring multiple copies of β and γ HC mRNA together, leading to foci formation and colocalization of β and γ HC mRNAs (Fig. 2*A*).

In this model, blocking HC translation should disrupt the formation and colocalization of *Dnah5* and *Dnah9* mRNA foci. To target ODA HC translation specifically, we used translation blocking morpholinos, which bind to target sequences and interfere with translation initiation through steric hindrance without affecting mRNA levels (25, 26). We targeted the translation of the γ-chain Dnah5, a common component of multiple types of ODAs that interact with β-chains Dnah9 and Dnah11 (27), together with Dnah5l, a duplicated ortholog that is also expressed in the zebrafish PND (28). Morphants (morpholino knockdown embryos) displayed classic phenotypes caused by defective motile cilia in zebrafish, including randomized heart placement along the left–right axis, ventral body curvature, and kidney cysts, while embryos injected with a nontargeting control morpholino appeared normal (*SI Appendix*, Fig. S2 *A–C*). As expected, the levels of *dnah5* and *dnah9* mRNA were comparable between morphants and controls by quantitative RT-PCR (RT-qPCR) using whole embryo lysates (Fig. 2*B*). We verified that ciliary motility was defective with cilia beating frequency reduced from 61.81 Hz ± 0.65 in controls to 13.25 ± 1.39 in morphants, and ODA number was reduced from 8.30 ± 0.13 to 2.91 ± 0.18 (*SI Appendix*, Fig. S2 *D–G* and Movie S2, Mean ± SEM). Since Dnah5 is required for Dnah9 trafficking to cilia (27), we sought additional validation by performing immunofluorescence staining for Dnah9. In *dnah5/5l* morphants, Dnah9 protein was diminished in cilia, and interestingly, cytosolic foci were reduced as well (*SI Appendix*, Fig. S2*H*). We then performed fluorescence in situ hybridization for *dnah5* and *dnah9* mRNA. Strikingly, not only *dnah5*, but also *dnah9* mRNA signals became more dispersed in morphants (Fig. 2*C*). We used the PND membrane marker anti-Cdh17 (15) to outline the PND in mounted embryos, performed image segmentation on projections of Z-stacks and measured the size and density of mRNA foci. Results indicated that the size of mRNA foci was significantly reduced, while the density of RNA foci significantly increased in morphants, suggesting a change of mRNA localization pattern (Fig. 2 *D* and *E*). Moreover, colocalization between *dnah5* and *dnah9* mRNAs was lost, with the average Pearson correlation coefficient reduced from 0.63 in control siblings to 0.07 in morphants (Fig. 2 *F* and *G* and Movie S3). These results are consistent with the above puromycin treatment results and support the hypothesis that translation of HCs and interactions between nascent HCs brings multiple molecules of encoding mRNAs into concentrated foci (Fig. 2*A*). Blocking of HC translation would thus prevent HC mRNA aggregation, leading to smaller but more HC mRNA foci, although we could not rule out the possibility that tubule dilation contributed to the disruption of foci formation.

Our model also predicts that the time course of HC mRNA foci formation and colocalization would correlate with multiciliogenesis. We therefore examined HC mRNA foci at multiple timepoints. Results showed that in the middle region of the PND, *dnah5* and *dnah9* mRNA foci were small and showed limited colocalization at the 20-somite stage (*SI Appendix*, Fig. S2*I*). Both foci size and colocalization increased at 25 hpf and persisted at 36 hpf and 48 hpf. The pattern in the anterior region was similar but lagged in time with colocalization evident by 36 hpf (*SI Appendix*, Fig. S2*I*). By contrast, *dnah5* and *dnah9* mRNA foci remained small and did not show colocalization at any timepoints in the posterior region (*SI Appendix*, Fig. S2*I*). Overall, the dynamic patterns of HC mRNA foci in different regions correlate with the progression of multiciliogenesis in the PND.

Combined, these results support the hypothesis that active translation of HCs leads to aggregation and colocalization of mRNAs encoding interacting HCs, which further increases the local concentration of nascent HCs (Fig. 2*A*).

**HC Translation Leads to the Enrichment of Ruvbl1, Ruvbl2, and Lrrc6 Into the HC Ribonucleoprotein Foci.** We previously identified Ruvbl1/Pontin and Ruvbl2/Reptin as cochaperones essential for dynein arm assembly and found them enriched in round foci in the cytosol of motile ciliated cells, together with Lrrc6, a DNAAF associated with the motile ciliopathy primary ciliary dyskinesia (PCD) (15, 16). We termed these foci "Ruvbl1/Ruvbl2 Hubs for Axonemal Dynein" (R2HADs) here. We first asked whether the Dnah9 ribonucleoprotein (RNP) foci and R2HADs represented the same compartment. Since antibodies against Ruvbl1 and Dnah9 were both generated in rabbits, we utilized GFP-tagged Ruvbl1, which we previously showed capable of rescuing *ruvbl1* mutants (16). We expressed Ruvbl1-GFP by injecting mRNA into zebrafish embryos at the 1-cell stage, fixed embryos at 1 d post fertilization (dpf) and performed immunofluorescence staining. We found that Dnah9 foci overlapped with a proportion of Ruvbl1-GFP foci (47.9%, Fig. 3*A*), indicating that at least a subset of R2 foci contain translating Dnah9. As motile ciliated cells produce multiple types of ODAs and IDAs, Dnah9-negative Ruvbl1 foci may represent translation sites of other HCs.

We then investigated whether endogenous R2 foci formation correlated with multiciliogenesis by performing immunostaining with anti-Ruvbl1 and anti-Ruvbl2. The specificity of the antibodies was validated in our previous studies by the absence of signals in corresponding loss-of-function mutants (15, 16). Results here showed that at the 20-Somite stage, Ruvbl1 foci were small in all regions of the PND (*SI Appendix*, Fig. S3*A*). They became most prominent in the middle region, especially at 25 hpf, but remained minimal in the posterior region, consistent with the status of multiciliogenesis. Ruvbl2 foci showed a very similar pattern (*SI Appendix*, Fig. S3*B*).

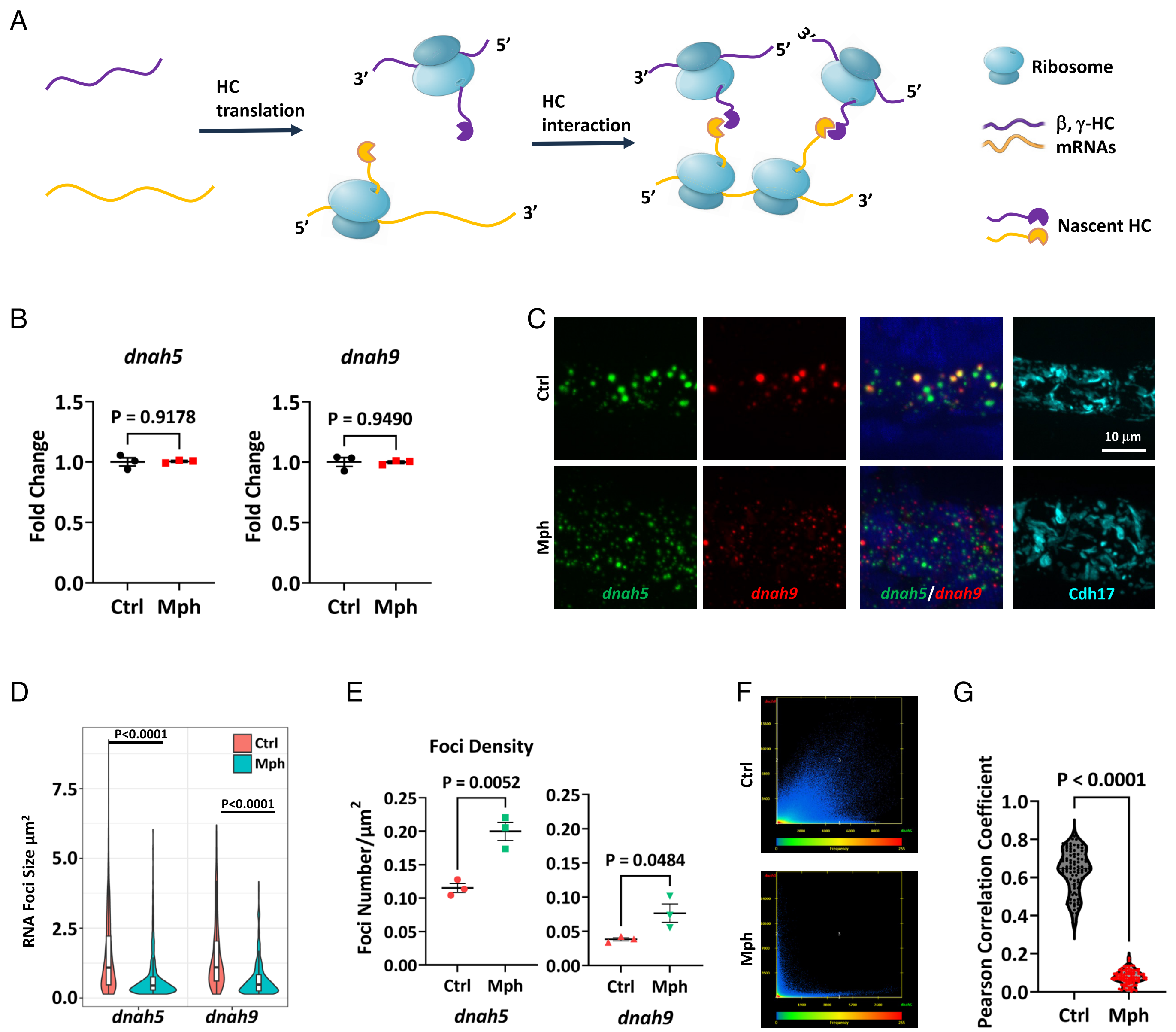

**Fig. 2.** HC mRNA foci formation and colocalization is disrupted in *dnah5/5l* morphants at 23.5 hpf. (*A*) A model depicting translating and interacting β and γ-HCs bringing multiple molecules of encoding mRNAs together. (*B*) Levels of *dnah5* and *dnah9* mRNA measured by RT-qPCR of embryo lysates. n = 3 biological replicates, pools of 20 or more embryos each. (*C*) Z-projections showing distribution patterns of *dnah5* (green) and *dnah9* (red) mRNA. PND in cyan by Cdh17. DAPI in blue. (*D*) RNA foci size and (*E*) density (pooled from three embryos per condition). (*F*) Z-projection of scatter plots of pixel intensity. (*G*) Pearson correlation coefficients between *dnah5* and *dnah9* mRNA signal (pooled slices of three embryos per condition). Ctrl: siblings injected with control morpholino; Mph: *dnah5/5l* morphants.

To directly test whether the formation of R2HADs was dependent on active protein translation, we injected puromycin into zebrafish embryos to block protein translation (as above) and performed immunofluorescence staining with anti-Lrrc6, the specificity of which was verified in our prior study by its absence in *lrrc6* mutants (20). While Lrrc6 was localized in cytosolic foci in control embryos, these foci were abolished after 15 min in puromycin-treated embryos, and this change in localization was prevented by coinjection with cycloheximide or emetine (Fig. 3 *B* and *C*), indicating that active translation is required for R2HAD formation. We also examined whether R2HADs were affected by targeted blocking of Dnah5 translation. Indeed, Ruvbl1, Ruvbl2, and Lrrc6 foci were reduced in *dnah5/dnah5l* morphants, while the levels of the proteins in whole embryo lysates remained unchanged as shown by western blot (Fig. 3 *D*–*G*), supporting the role of HC translation in recruiting R2HAD components.

**Ruvbl1 Functions Downstream of HC RNP Foci Formation But Upstream of Lrrc6 Foci Formation.** To determine the molecular function of R2HAD components in HC mRNA-nascent peptide foci formation, we utilized zebrafish mutant alleles isolated in an insertional mutagenesis screen (19). Previously we showed that *hi1055B* is a loss-of-function allele of *ruvbl1* (16). Here, we first examined the impact of *ruvbl1* inactivation on the localization pattern of *dnah5* and *dnah9* mRNA by fluorescence in situ hybridization. Results showed that *dnah5* and *dnah9* mRNA foci and colocalization persisted in *ruvbl1*$^{hi1055B/hi1055B}$ mutants compared to sibling controls (Fig. 4*A*). The average Pearson correlation coefficients between signals of *dnah5* and *dnah9* mRNA were 0.65 and 0.66 in mutants and controls, respectively, and not statistically different (Fig. 4 *B* and *C* and Movie S4). We additionally investigated the localization pattern of Dnah9 protein by immunofluorescence staining. Cytosolic Dnah9 foci remained

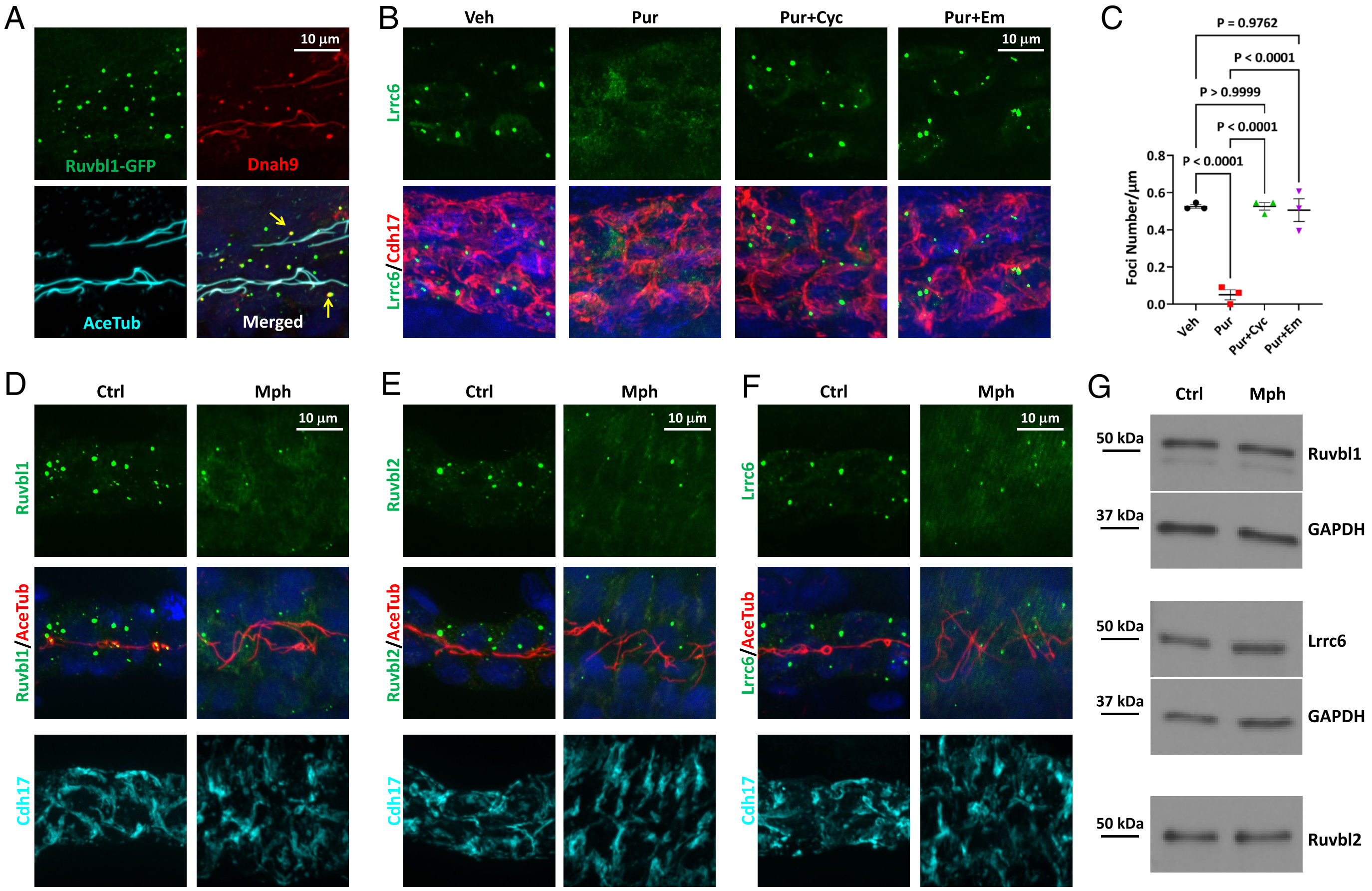

**Fig. 3.** R2HADs are RNPs initiated by translating HCs. (*A*) Colocalization of Ruvbl1-GFP (green) foci with Dnah9 protein (red) foci at 25 hpf shown by Z-projections. Examples indicated by arrows. Cilia indicated by AceTub (cyan). (*B*) Cytosolic foci of Lrrc6 (green) are sensitive to puromycin treatment as shown by Z-projections. Embryos were processed at 26 hpf. Cdh17 in red labels PND cells. (*C*) Quantification of Lrrc6 foci normalized by the length of PND analyzed. (*D*–*F*) Foci of Ruvbl1 (green in *D*), Ruvbl2 (green in *E*), and Lrrc6 (green in *F*) are reduced in *dnah5/5l* morphants at 23.5 hpf. Cilia are indicated by AceTub in red and PND cells are labeled by anti-Cdh17 in cyan. (*G*) Western blot of R2HAD components using total embryo lysates. Ruvbl1 and Lrrc6 are detected with direct western, and GAPDH from the same blot was used as a loading control. Ruvbl2 is detected by immuno-precipitation followed by western using aliquots of the same lysates used in direct western. AceTub: anti-acetylated-tubulin signal; Ctrl: siblings injected with control morpholino; Mph: *dnah5/5l* morphants; Veh: vehicle; Pur: puromycin; Pur+Cyc: puromycin and cycloheximide; Pur+Em: puromycin and emetine.

in *ruvbl1*$^{hi1055B/hi1055B}$ mutants, despite greatly diminished Dnah9 signal in cilia (*SI Appendix*, Fig. S4*A*).

We then asked whether Ruvbl1 and Lrrc6 are interdependent for foci formation. In the PND cells of *ruvbl1*$^{hi1055B/hi1055B}$ mutants, Lrrc6 signal became diffusive, in contrast to the punctate pattern in control siblings (Fig. 4*D*). By contrast, in *lrrc6*$^{hi3308/hi3308}$ mutants, which were loss-of-function mutants as shown previously (20), Ruvbl1 foci persisted (Fig. 4*E*).

Together, these results suggest that Ruvbl1 functions downstream from the formation of HC ribonucleoprotein foci but upstream of the recruitment of Lrrc6.

**Ruvbl1, Ruvbl2, and Lrrc6 Function Cotranslationally.** To investigate whether Ruvbl1 functions cotranslationally, we examined the sensitivity of Dnah9 foci to puromycin treatment in *ruvbl1* mutants. Interestingly, Dnah9 foci persisted 15 min after puromycin treatment in *ruvbl1*$^{hi1055B/hi1055B}$ mutants, and residual foci were still detected 30 min after injection, whereas foci were dispersed in control siblings (Fig. 5*A* and *SI Appendix*, Fig. S5*A*). We expanded this analysis to two DNAAF genes associated with PCD (PCD-DNAAFs), *lrrc6* and *pih1d3*. Similar to *ruvbl1*$^{hi1055B/hi1055B}$ mutants, ciliary localization of Dnah9 was disrupted, while cytosolic foci persisted (*SI Appendix*, Fig. S4 *B* and *C*) in both *lrrc6*$^{hi3308/hi3308}$ and *pih1d3*$^{hi1392/hi1392}$, another loss-of-function mutant isolated in the same genetics screen and characterized in our prior studies (12, 19). Dnah9 foci became resistant to puromycin treatment in *lrrc6*$^{hi3308/hi3308}$ mutants (Fig. 5B and *SI Appendix*, Fig. S5*B*), whereas foci in *pih1d3*$^{hi1392/hi1392}$ mutants remained sensitive to puromycin and dispersed as in their control siblings (Fig. 5C and *SI Appendix*, Fig. S5*C*). This result is consistent with the physical interaction between Lrrc6 and Ruvbl2 we identified previously (15), placing Lrrc6 in a very early step in axonemal dynein assembly, consistent with a previous study that implicated Lrrc6 in a chaperone relay of HC assembly (29).

It is possible that fully synthesized Dnah9 was misfolded and formed aggregates resistant to puromycin treatment in R2HAD (*ruvbl1*, *ruvbl2,* and *lrrc6*) mutants. Alternatively, Dnah9 translation could be stalled and therefore resistant to puromycin incorporation (Fig. 5*D*). To test the latter, we quantified translating HC mRNAs in response to puromycin treatment. We first confirmed that the levels of total *dnah5* and *dnah9* mRNA were not significantly different in *ruvbl1*$^{hi1055B/hi1055B}$ and *pih1d3*$^{hi1392/hi1392}$ mutants compared to their sibling controls and remained unchanged by acute puromycin treatment using RT-qPCR (Fig. 5 *E* and *F* and *SI Appendix*, Fig. S5 *D* and *E*, total lysate). We then used immunoprecipitation with anti-RPL19, a ribosome component, to pull down translating mRNA from total lysates and quantified the amount of pulled-down *dnah5* and *dnah9* mRNA using RT-qPCR. While control IgG failed to pull down

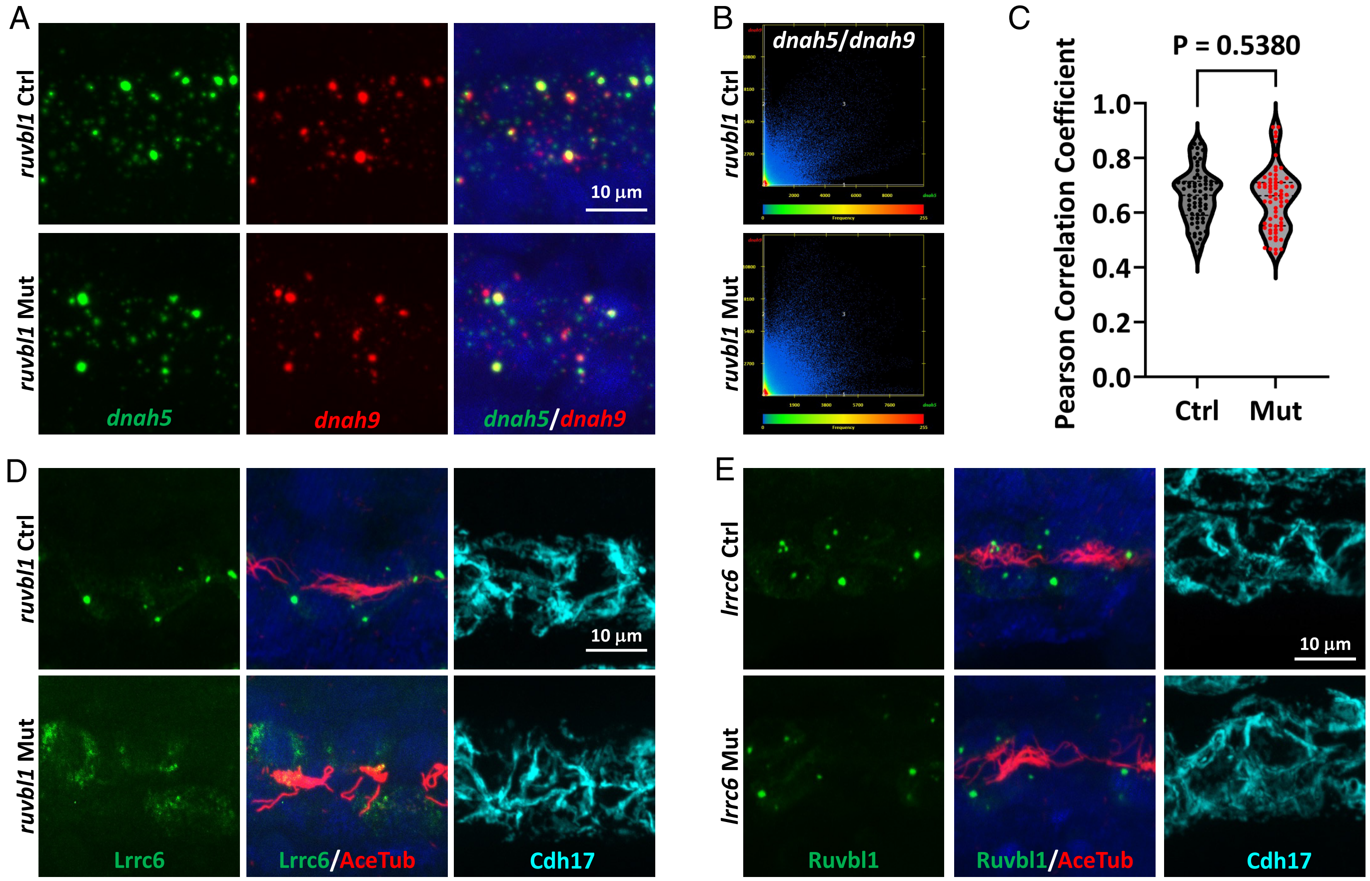

**Fig. 4.** Ruvbl1 functions between Dnah9 foci formation and Lrrc6 recruitment. (*A*) *dnah5* (green) and *dnah9* (red) mRNA foci and colocalization persist in *ruvbl1* mutant PND at 25 hpf shown by projections of Z-stacks. (*B*) Z-projections of scatter plots of pixel intensity between two mRNAs. (*C*) Pearson correlation coefficient between signals of two mRNAs in *ruvbl1* mutants and control siblings. Pooled from slices of Z-stacks of three embryos per condition. (*D*) Lrrc6 (green) distribution pattern in *ruvbl1* mutant PND in comparison to sibling controls at 27 hpf. Cilia indicated by AceTub in red. (*E*) Ruvbl1 (green) distribution pattern in *lrrc6* mutant PND in comparison to sibling controls at 27 hpf. Cilia indicated by AceTub in red. AceTub: anti-acetylated-tubulin signal; Ctrl: control; Mut: mutant.

*dnah5* and *dnah9* mRNA, anti-RPL19 isolated sufficient *dnah5* and *dnah9* mRNA for RT-qPCR analysis. As expected, in control sibling embryos the amount of translating *dnah5* and *dnah9* mRNA was significantly reduced by puromycin treatment (Fig. 5*E* and *SI Appendix*, Fig. S5*D*, pull down). This reduction was diminished in *ruvbl1*$^{hi1055B/hi1055B}$ mutants (Fig. 5*E* and *SI Appendix*, Fig. S5*D*, pull down), supporting a cotranslational function of R2HADs. In contrast, the amount of translating *dnah5* and *dnah9* mRNA was reduced in *pih1d3*$^{hi1392/hi1392}$ mutants by puromycin treatment, similar to control siblings (Fig. 5*F* and *SI Appendix*, Fig. S5*E*, pull down), suggesting that *pih1d3* functions downstream of cotranslational HC assembly (Fig. 5*D*).

Combined, these results support a model of multistep axonemal dynein assembly (Fig. 5*D*), where R2HAD components Ruvbl1, Ruvbl2, and Lrrc6 are involved in a cotranslational step, albeit downstream of HC ribonucleoprotein foci formation mediated by inter-HC interaction via the N-terminal region. By contrast, Pih1d3 functions further downstream, leaving translating HC sensitive to puromycin treatment.

**Both Stable and Weak Interactions Contribute to HC-R2HAD Formation.** To probe the biophysical properties of R2HADs, we treated zebrafish embryos with 1,6-hexanediol, an aliphatic compound known to disrupt weak hydrophobic protein–protein and protein–RNA interactions, and frequently used to dissolve phase-separated liquid droplets (30–34). After 30 min of treatment, the size and number of Dnah9 foci remained unchanged, along with the ciliary signal of Dnah9 (Fig. 6*A* and *SI Appendix*, Fig. S6*A*). By contrast, Ruvbl1, Ruvbl2, and Lrrc6 foci appeared dispersed but still granular (Fig. 6 *B*–*D*). In treated samples, many seemingly granular structures were not detected by automatic segmentation, and the size of segmented objects was reduced significantly (*SI Appendix*, Fig. S6 *B*–*D*). The sensitivity of Ruvbl1, Ruvbl2, and Lrrc6 foci to 1,6-hexanediol treatment, compared to the resistance of Dnah9 foci, support a model where a stable core, consisting of translating HCs tethered to the encoding mRNA through ribosomes, initiates molecular condensation of cochaperones and DNAAFs through transient and weak interactions. While the stable core and mature HC already trafficked to cilia are resistant to the acute 1,6-hexanediol treatment, the interaction of Ruvbl1, Ruvbl2, and Lrrc6 with the core is sensitive (Fig. 6*E*). Whether the interaction between β and γ HCs is sensitive to 1,6-hexanediol remains unknown. However, the size of the scaffold, consisting of a 14 K mRNA and multiple copies of ribosomes and nascent HCs, would limit its diffusion.

## Discussion

The synthesis and assembly of large and interacting proteins, such as axonemal HCs, poses a significant challenge for the cell. To put this into context, differentiated multiciliated epithelial cells in the zebrafish PND display up to 16 motile cilia per cell, each measuring 9 μm in length (21). The ODAs decorate each of the 9 microtubule doublets every 24 nm along the length of the motile cilium, thus approximately 54 K ODAs are manufactured per cell from 19 hpf to 48 hpf (*SI Appendix*, Fig. S1*C*) (21). Despite the

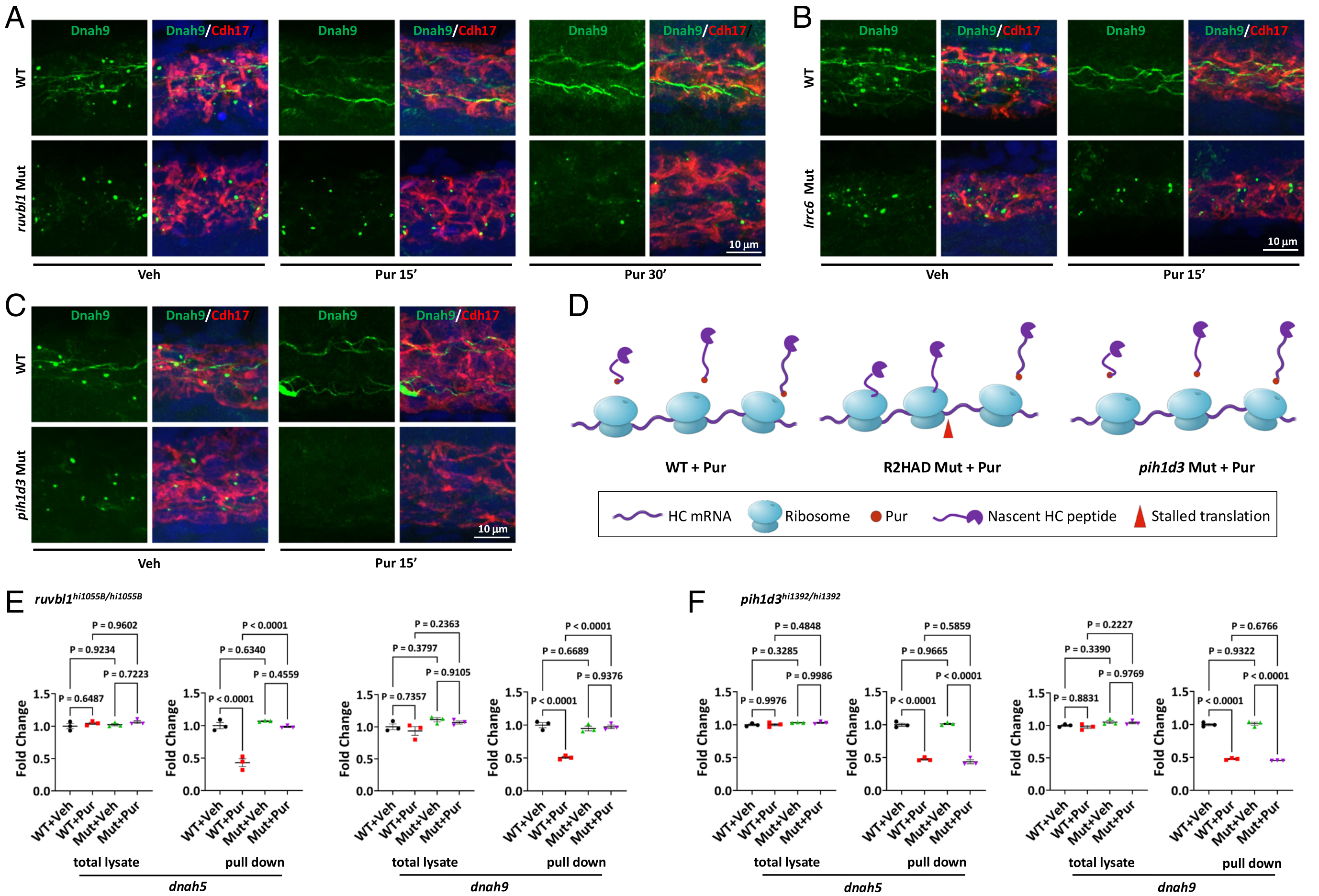

**Fig. 5.** R2HAD is a cotranslational hub for dynein arm assembly. (*A*–*C*) Sensitivity of Dnah9 (green) foci to puromycin treatment in *ruvbl1* (*A*), *lrrc6* (*B*), and *pih1d3* (*C*) mutants as shown by Z-projections. Cdh17 in red labels the PND. Embryos were processed at 26 hpf. (*D*) A model depicting stalled translation of HCs, hence resistance of HC foci to puromycin treatment, in R2HAD but not *pih1d3* mutants. (*E* and *F*) The level of translating *dnah5* and *dnah9* mRNA in *ruvbl1* and *pih1d3* mutants treated with vehicle or puromycin shown by RT-qPCR. n = 3 technical repeats using 120 embryos each. A biological repeat is shown in *SI Appendix*, Fig. S5 *D* and *E*. Unit 1 is defined as the expression level in control siblings treated with vehicle. WT: wild type siblings; Mut: mutant; Veh: vehicle; Pur: puromycin.

daunting task of finding proper binding partners in the crowded cytosol, while preventing aggregate formation of highly concentrated nascent HCs, efficient and accurate assembly of dynein arms is achieved by every motile ciliated cell.

Our study unravels the pivotal role of cotranslational recruitment of chaperones and assembly factors as an initial and indispensable step in orchestrating the production and assembly of axonemal dynein. We show that HC and R2HAD foci are initiated by the stable attachment between translating HCs and encoding mRNAs through ribosomes, and interactions between the N terminus of HCs (Fig. 6*E*). In contrast to *dnah9* mRNA, *dnai1.2*, *dnai2b,* and *dnal1* mRNA showed no significant colocalization with *dnah5* mRNA, suggesting that the interactions between HCs with ICs or LCs may occur post-HC translation.

Since R2HAD represents a cytosolic entity with concentrated specific components, it fits the simplest definition of biomolecular condensate (35, 36). Instead of being mainly driven by weak interactions, polysome mRNA decorated with nascent interacting HCs appears to form a percolated network and initiate R2HAD formation, consistent with a form of molecular condensation called phase separation coupled to percolation (36). The characteristics of DNAAF foci observed previously, including their shape, fission and fusion, and mobility of molecules within (18), are also consistent with our model of molecular condensation initiated by large stable scaffolds. Moreover, the rapid dispersion of R2HADs when translation is aborted by puromycin treatment in our study underscores the importance of stable interactions between nascent peptide chains and mRNAs, but is less compatible with foci formation driven mainly by component concentration reaching saturation (35, 37).

Although cotranslational assembly is increasingly recognized as a mechanism for protein complex formation (38–45), cotranslational molecular condensation of cochaperones and assembly factors has not been shown before for axonemal dynein and provides a mechanism connecting translation, folding, and assembly. We propose that instead of concentrating components to speed up axonemal dynein biogenesis, R2HAD foci formation is a result of active translation, supported by our finding that Ruvbl1 is dispensable for HC RNP foci formation and consistent with the concept of a dynein arm factory proposed by a recent opinion article (5). Subsequent molecular condensation of chaperones and DNAAFs ensures the dynamics and fluidity of highly concentrated nascent HCs by facilitating cotranslational folding and assembly. Interestingly, mRNAs encoding a HC of cytoplasmic dynein, and several nondynein proteins are also found in cytoplasmic foci that are sensitive to puromycin treatment (46), suggesting a more widespread role of nascent peptides in aggregating mRNA.

Clinically, defective ciliary motility underlies PCD. PCD patients develop progressive lung disease characterized by mucus impaction, recurrent sinopulmonary infections, and accelerated lung function decline originating from impaired mucociliary clearance (47, 48). Male infertility and laterality defects of internal organ placements are also frequent findings in PCD patients. Currently there is no

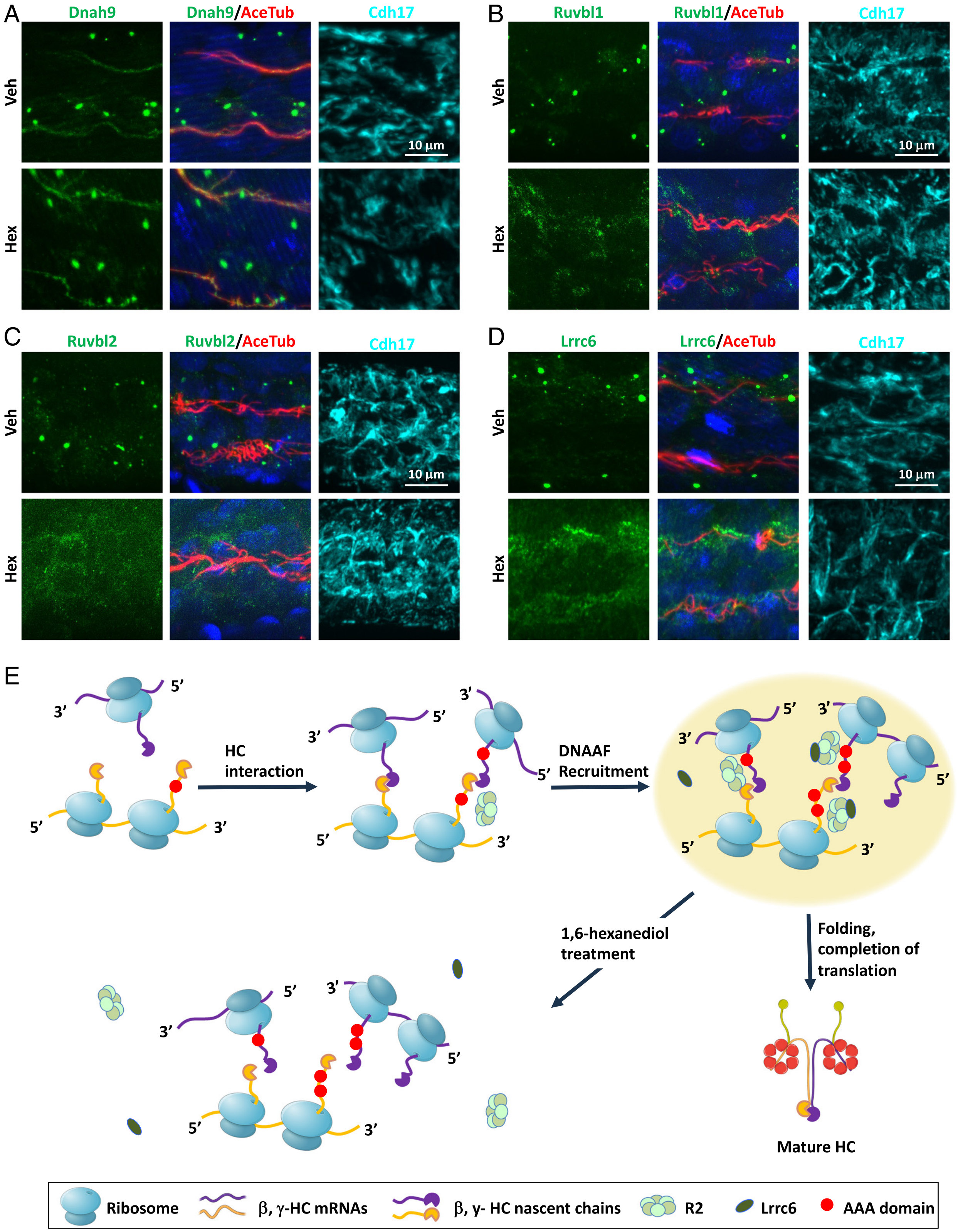

**Fig. 6.** Both stable and weak interactions contribute to R2HAD formation. (*A*–*D*) Response of Dnah9 (*A*), Ruvbl1 (*B*), Ruvbl2 (*C*), and Lrrc6 (*D*) foci to 1,6-hexanediol treatment shown by Z-projections. Embryos were processed at 26 hpf. Cilia indicated by AceTub in red. PND in cyan by Cdh17. DAPI in blue. (*E*) A model of R2HAD formation and function that incorporates steps depicted in Figs. 2*A* and 5*D*. Active HC translation leads to high local concentration of HC nascent peptides. Physical interactions between the N-terminal regions of nascent β- and γ-HCs bring multiple copies of mRNAs together, forming a stable core, which recruits R2 via weaker interactions, followed by Lrrc6. R2 and Lrrc6 function cotranslationally to allow the folding and completion of HC translation. 1,6-hexanediol disrupts the interaction of R2 and Lrrc6 with the core, but not HC polysomes. AceTub: acetylated-tubulin; Veh: vehicle; Hex: 1,6-hexanediol.

specific therapy for PCD and management of symptoms, including improving mucus clearance and treating recurrent infections, has been the main approach. Our results provide a molecular framework and readouts, from RNA localization to R2 foci formation and sensitivity to translation inhibition, for dissecting the precise molecular functions of PCD-DNAAFs and identifying potential therapeutic targets. Moreover, the connection between translation, folding, and assembly raises the intriguing possibility that a subset of PCD syndromes, specifically those caused by partial loss-of-function mutations in DNAAFs, could be ameliorated by reducing translation rate. Treatment with chemical chaperones, suggested by a previous study (29), may also be beneficial.

Ruvbl1 and Ruvbl2 are closely related AAA ATPases that interact and function as cochaperones, facilitating the assembly of multiple protein complexes (49–51). Additionally, they play critical roles in the formation of multiple RNPs, including the stress granule (52) and snoRNPs (53). A recent study found that in *Drosophila*, Ruvbl1 and Ruvbl2 are localized to RNPs containing mRNAs encoding testis-specific dynein HCs (54). However, knockdown of *Ruvbl1* and *Ruvbl2* via RNAi disrupted the formation of HC mRNA clusters (54), in contrast to our finding that HC mRNA foci persist in the PND of zebrafish *ruvbl1* mutants. Since in *Drosophila* sperm, flagella form through a unique cytosolic pathway distinct from intraflagellar transport-dependent compartmentalized ciliogenesis (55–57), it is thought that the formation and localization of these granules allow for efficient incorporation of HCs into the growing axoneme in the cytosol (54). It will be interesting to investigate whether Ruvbl1 and Ruvbl2 have additional cotranslational function in this system.

In summary, we propose that axonemal dynein folding and assembly commence cotranslationally, accompanied by molecular condensation of chaperones and assembly factors. Our findings define key components of an early cotranslational hub that facilitates the assembly process, and raise intriguing questions, for example, whether ribosome pausing is involved, whether there are sequence features to allow for coordinated translation, and how RNA entanglement is prevented. Importantly, the synthesis of other large proteins poses similar challenges, and it is attractive to propose that our model may be employed as a more general mechanism to ensure efficient folding and prevent aggregate formation.

## Materials and Methods

**Materials.** Materials used in the study, including antibodies, fish strain, genetic mutants, commercial assays and kits, chemicals, oligos, morpholinos, and software are listed in the "Key Sources Table" in *SI Appendix*.

**Zebrafish Husbandry.** Zebrafish were of the TU/AB background and were maintained according to standard protocols (58). Embryos were obtained through natural spawning.

**Molecular Cloning.** The full-length coding sequence of *ruvbl1* and fragments of *dnah5*, *dnah9*, *dnai1.2*, *dnai2b*, *dnal1* were PCR amplified from a zebrafish cDNA pool using oligos listed in the Key Resources Table, subcloned into vectors and verified by sequencing. More details in *SI Appendix*.

**RNA Probe Synthesis.** RNA probes were synthesized via in vitro transcription using T7 RNA polymerase with DIG or Fluorescein RNA labeling mix. More detailed procedures and coverage of each probe in *SI Appendix*.

**Immunofluorescence Staining.** Zebrafish embryos fixed in Dent's fixative (80% methanol/20% DMSO) were incubated in primary antibody, followed by secondary antibody, deyolked manually, flat mounted, and imaged. More detailed procedures in *SI Appendix*. Antibodies used were specified in the Key Resources Table in *SI Appendix*.

**Fluorescence In Situ Hybridization Coupled with Immunostaining.** A previous published protocol was followed (59). Zebrafish embryos fixed with 4% paraformaldehyde were subjected to in situ hybridization procedures first, followed by immunostaining. More details in *SI Appendix*.

**Pixel-Based Colocalization Analysis in Zen Blue (Figs. 1 *C* and *D*, 2 *F* and *G*, and 4 *B* and *C*).** The "Colocalization" tool in Zen Blue was used to analyze the potential overlap between two RNA signals. Optimal thresholds were determined automatically using the "Costes" function based on a statistical method described before (60). Z-projection of scatter plots were generated in ImageJ. More details in *SI Appendix*.

**Microinjection.** Microinjection was performed as described previously (61). Briefly, mRNA synthesized in vitro or morpholino oligos were injected into zebrafish embryos at the one cell stage. Injected embryos were incubated, followed by analysis at later stages. More details in *SI Appendix*.

**RT-qPCR.** Total RNA was extracted from zebrafish embryos. cDNA was synthesized and used as template for RT-qPCR. More detailed procedures in *SI Appendix*. Primers listed in the Key Resources Table in *SI Appendix*.

**Ciliary Motility Analysis.** High-speed DIC videomicroscopy recordings of the pronephric duct cilia were acquired at ~492 Hz for ~1 s. Kymographs and analysis of the ciliary beating frequency (CBF) were done using Fiji (62). More detailed procedures in *SI Appendix*.

**Electron Microscopy.** Zebrafish embryos at 48hpf were fixed, partially dissected, embedded, and poststained. Grids were viewed in a FEI Tecnai G2 Spirit BioTWIN transmission electron microscope, and images were captured. More detailed procedures in *SI Appendix*.

**Puromycin, Cycloheximide, and Emetine Treatment.** Embryos at 26 hpf were collected. Vehicle, puromycin, puromycin in combination with cycloheximide or emetine were injected into the brain ventricle. 15 min after injection, embryos were fixed in Dent's fixative. More detailed procedures in *SI Appendix*.

**Quantification of RNA Foci Size and Density (Fig. 2 *D* and *E*).** MATLAB was used to quantify the size and density of RNA foci. The region of interest (ROI) in each image was identified using the anti-Cdh17 immunostaining signal, which labels the membrane of pronephric duct cells. Marker-controlled watershed segmentation was then used to segment *dnah5* and *dnah9* mRNA foci in the ROI.

The size and number of RNA foci segments identified within the ROI were quantified. RNA foci density was defined as RNA segment number divided by ROI size.

More detailed procedures in *SI Appendix*.

**Automated Segmentation and Quantification of Protein Foci (Fig. 3*C* and *SI Appendix*, Figs. S1*E*, S5 *A–C*, and S6 *A–D*).** The LabKit plugin in Fiji was used to segment and quantify protein foci automatically (63). A pixel classifier was trained with positive and background regions and used to segment foci automatically. More details in *SI Appendix*.

**Protein Extraction, Immunoprecipitation, SDS-PAGE, and Western Blot.** Zebrafish embryos were lyzed and protein concentration of lysates was measured. Equal amounts of total protein were used for subsequent analysis. For Ruvbl2, immunoprecipitation was performed using anti-Ruvbl2. For Ruvbl1 and Lrrc6, total lysates were used. Samples were run on a SDS-PAGE gel, transferred, and detected with western blot. For Ruvbl1 and Lrrc6, GAPDH on the same blot was used as a loading control. While cropped images were used in Fig. 3*G*, the original images are presented in *SI Appendix*, Fig. S7. More details in *SI Appendix*.

**Ribosome Pull Down.** A STAR protocol was followed (64). Briefly, translating mRNAs were pulled down from zebrafish embryo lysates using anti-RPL19, followed by RNA extraction and cDNA synthesis. More details in *SI Appendix*.

**Hexanediol Treatment.** Embryos at 26 hpf were incubated in 5% hexanediol for 30 min, and then immediately fixed in Dent's fixative. More details in *SI Appendix*.

**Statistical Analysis.** Figs. 2 *B*, *D*, *E*, and *G* and 4*C* and *SI Appendix*, Figs. S2 *E* and *G*, S5 *A–C*, and S6 *A–D* were analyzed by the unpaired two-tailed *t* test. Figs. 1*D*, 3*C*, and 5 E and F and *SI Appendix*, Figs. S1*E* and S5 *D* and *E* were analyzed using one-way ANOVA followed by Tukey's multiple-comparison test using GraphPad Prism 9 software. All data are presented as mean ± SEM.

**Animal Care Ethics.** Zebrafish experiments were conducted in Yale University School of Medicine in accordance with the guidelines of Yale University Institutional Animal Care and Use Committee (IACUC). Protocols were approved by IACUC (Protocol No. 2021-10778).

**Data, Materials, and Software Availability.** Code data have been deposited in GitHub (65). All other data are included in the manuscript and/or supporting information.

**ACKNOWLEDGMENTS.** We thank Zhongyuan Zuo and the Yale Center for Cellular and Molecular Imaging Electron Microscopy Facility for sample processing, technical support, and image acquisition; Gizem Goles and Seiji Nakanishi for maintaining fish; Professor Takeda for the gift of anti-Dnah9; Arthur Horwich for critical reading of the manuscript; the Brueckner lab for helpful discussions; and Caterina Di Pietro for assistance with model illustration. Research in the Sun lab is supported by grants from NIH (R56HL168089, 1R01HL175156, and DK113135 to Z.S.) and a Discovery Award from Peer Reviewed Medical Research Program (HT9425-23-1-0020 to Z.S.). S.W. was partly supported by NIH (UG3CA268202, U01CA260701, R01HG011245, DP2GM137414, and R33CA251037) and Pershing Square Sohn Cancer Research Alliance. Y.C. was in part supported by the China Scholarship Council. L.D. was supported by a Career Development Award from the American Heart Association (23CDA1050794). S.Y. was supported by grants from NIH (5R01HL165241) and the American Heart Association (940516, 969048, and 24IPA1275767).

---

Author affiliations: [a]Department of Genetics, Yale University School of Medicine, New Haven, CT 06510; [b]Cardiovascular Research Center, Cardiology Division, Department of Medicine, Massachusetts General Hospital and Harvard Medical School, Boston, MA 02129; [c]Division of Pulmonary, Critical Care, and Sleep Medicine, Yale University School of Medicine, New Haven, CT 06520; and [d]Department of Cell Biology, Yale University School of Medicine, New Haven, CT 06510

Author contributions: S.Y., S.W., and Z.S. designed research; Y.L., W.X., L.D., and C.Z. performed research; Y.C. and S.W. contributed new reagents/analytic tools; Y.L., W.X., Y.C., L.D., S.Y., and S.W. analyzed data; A.L.C. and C.J.B. discussed ideas; and Y.L., Y.C., L.D., A.L.C., C.J.B., S.Y., S.W., and Z.S. wrote the paper.

1. J. A. Whitsett, T. Alenghat, Respiratory epithelial cells orchestrate pulmonary innate immunity. *Nat. Immunol.* **16**, 27–35 (2015).
2. A. K. Fok, H. Wang, A. Katayama, M. S. Aihara, R. D. Allen, 22S axonemal dynein is preassembled and functional prior to being transported to and attached on the axonemes. *Cell Motil. Cytoskeleton* **29**, 215–224 (1994).
3. M. E. Fowkes, D. R. Mitchell, The role of preassembled cytoplasmic complexes in assembly of flagellar dynein subunits. *Mol. Biol. Cell* **9**, 2337–2347 (1998).
4. S. M. King, Axonemal dynein arms. *Cold Spring Harb. Perspect. Biol.* **8**, a028100 (2016).
5. S. M. King, Cytoplasmic factories for axonemal dynein assembly. *J. Cell Sci.* **134**, jcs258626 (2021).
6. C. P. Diggle *et al.*, HEATR2 plays a conserved role in assembly of the ciliary motile apparatus. *PLoS Genet.* **10**, e1004577 (2014).
7. A. Horani *et al.*, Whole-exome capture and sequencing identifies HEATR2 mutation as a cause of primary ciliary dyskinesia. *Am. J. Hum. Genet.* **91**, 685–693 (2012).
8. A. Horani *et al.*, LRRC6 mutation causes primary ciliary dyskinesia with dynein arm defects. *PLoS ONE* **8**, e59436 (2013).
9. E. Kott *et al.*, Loss-of-function mutations in LRRC6, a gene essential for proper axonemal assembly of inner and outer dynein arms, cause primary ciliary dyskinesia. *Am. J. Hum. Genet.* **91**, 958–964 (2012).
10. H. M. Mitchison *et al.*, Mutations in axonemal dynein assembly factor DNAAF3 cause primary ciliary dyskinesia. *Nat. Genet.* **44**, 381–389 (2012).
11. D. J. Moore *et al.*, Mutations in ZMYND10, a gene essential for proper axonemal assembly of inner and outer dynein arms in humans and flies, cause primary ciliary dyskinesia. *Am. J. Hum. Genet.* **93**, 346–356 (2013).
12. C. Olcese *et al.*, X-linked primary ciliary dyskinesia due to mutations in the cytoplasmic axonemal dynein assembly factor PIH1D3. *Nat. Commun.* **8**, 14279 (2017).
13. H. Omran *et al.*, Ktu/PF13 is required for cytoplasmic pre-assembly of axonemal dyneins. *Nature* **456**, 611–616 (2008).
14. M. A. Zariwala *et al.*, ZMYND10 is mutated in primary ciliary dyskinesia and interacts with LRRC6. *Am. J. Hum. Genet.* **93**, 336–345 (2013).
15. L. Zhao *et al.*, Reptin/Ruvbl2 is a Lrrc6/Seahorse interactor essential for cilia motility. *Proc. Natl. Acad. Sci. U.S.A.* **110**, 12697–12702 (2013).
16. Y. Li, L. Zhao, S. Yuan, J. Zhang, Z. Sun, Axonemal dynein assembly requires the R2TP complex component Pontin. *Development* **144**, 4684–4693 (2017).
17. A. Horani *et al.*, Establishment of the early cilia preassembly protein complex during motile ciliogenesis. *Proc. Natl. Acad. Sci. U.S.A.* **115**, E1221–E1228 (2018).
18. R. L. Huizar *et al.*, A liquid-like organelle at the root of motile ciliopathy. *eLife* **7**, e38497 (2018).
19. Z. Sun *et al.*, A genetic screen in zebrafish identifies cilia genes as a principal cause of cystic kidney. *Development* **131**, 4085–4093 (2004).
20. N. Kishimoto, Y. Cao, A. Park, Z. Sun, Cystic kidney gene seahorse regulates cilia-mediated processes and Wnt pathways. *Dev. Cell* **14**, 954–961 (2008).
21. A. G. Kramer-Zucker *et al.*, Cilia-driven fluid flow in the zebrafish pronephros, brain and Kupffer's vesicle is required for normal organogenesis. *Development* **132**, 1907–1921 (2005).
22. Y. Liu, N. Pathak, A. Kramer-Zucker, I. A. Drummond, Notch signaling controls the differentiation of transporting epithelia and multiciliated cells in the zebrafish pronephros. *Development* **134**, 1111–1122 (2007).
23. M. Ma, Y. J. Jiang, Jagged2a-notch signaling mediates cell fate choice in the zebrafish pronephric duct. *PLoS Genet.* **3**, e18 (2007).
24. T. Walton, H. Wu, A. Brown, Structure of a microtubule-bound axonemal dynein. *Nat. Commun.* **12**, 477 (2021).
25. A. Nasevicius, S. C. Ekker, Effective targeted gene "knockdown" in zebrafish. *Nat. Genet.* **26**, 216–220 (2000).
26. A. Rossi *et al.*, Genetic compensation induced by deleterious mutations but not gene knockdowns. *Nature* **524**, 230–233 (2015).
27. N. T. Loges *et al.*, Recessive DNAH9 loss-of-function mutations cause laterality defects and subtle respiratory ciliary-beating defects. *Am. J. Hum. Genet.* **103**, 995–1008 (2018).
28. H. Yamaguchi, T. Oda, M. Kikkawa, H. Takeda, Systematic studies of all PIH proteins in zebrafish reveal their distinct roles in axonemal dynein assembly. *eLife* **7**, e36979 (2018).
29. G. R. Mali *et al.*, ZMYND10 functions in a chaperone relay during axonemal dynein assembly. *eLife* **7**, e34389 (2018).
30. J. R. Wheeler, T. Matheny, S. Jain, R. Abrisch, R. Parker, Distinct stages in stress granule assembly and disassembly. *eLife* **5**, e18413 (2016).
31. N. Shulga, D. S. Goldfarb, Binding dynamics of structural nucleoporins govern nuclear pore complex permeability and may mediate channel gating. *Mol. Cell. Biol.* **23**, 534–542 (2003).
32. K. Ribbeck, D. Gorlich, The permeability barrier of nuclear pore complexes appears to operate via hydrophobic exclusion. *EMBO J.* **21**, 2664–2671 (2002).
33. A. Molliex *et al.*, Phase separation by low complexity domains promotes stress granule assembly and drives pathological fibrillization. *Cell* **163**, 123–133 (2015).
34. S. Kroschwald *et al.*, Promiscuous interactions and protein disaggregases determine the material state of stress-inducible RNP granules. *eLife* **4**, e06807 (2015).
35. S. F. Banani, H. O. Lee, A. A. Hyman, M. K. Rosen, Biomolecular condensates: Organizers of cellular biochemistry. *Nat. Rev. Mol. Cell Biol.* **18**, 285–298 (2017).
36. T. Mittag, R. V. Pappu, A conceptual framework for understanding phase separation and addressing open questions and challenges. *Mol. Cell* **82**, 2201–2214 (2022).
37. D. T. McSwiggen, M. Mir, X. Darzacq, R. Tjian, Evaluating phase separation in live cells: Diagnosis, caveats, and functional consequences. *Genes. Dev.* **33**, 1619–1634 (2019).
38. A. Bernardini *et al.*, Hierarchical TAF1-dependent co-translational assembly of the basal transcription factor TFIID. *Nat. Struct. Mol. Biol.* **30**, 1141–1152 (2023), 10.1038/s41594-023-01026-3.
39. C. D. Duncan, J. Mata, Widespread cotranslational formation of protein complexes. *PLoS Genet.* **7**, e1002398 (2011).
40. I. Kamenova *et al.*, Co-translational assembly of mammalian nuclear multisubunit complexes. *Nat. Commun.* **10**, 1740 (2019).
41. K. Khan, P. L. Fox, Benefits of co-translational complex assembly for cellular fitness. *BioEssays* **45**, e2300024 (2023).
42. K. Khan *et al.*, Multimodal cotranslational interactions direct assembly of the human multi-tRNA synthetase complex. *Proc. Natl. Acad. Sci. U.S.A.* **119**, e2205669119 (2022).
43. E. Natan, J. N. Wells, S. A. Teichmann, J. A. Marsh, Regulation, evolution and consequences of cotranslational protein complex assembly. *Curr. Opin. Struct. Biol.* **42**, 90–97 (2017).
44. M. Seidel *et al.*, Co-translational assembly orchestrates competing biogenesis pathways. *Nat. Commun.* **13**, 1224 (2022).
45. A. Shiber *et al.*, Cotranslational assembly of protein complexes in eukaryotes revealed by ribosome profiling. *Nature* **561**, 268–272 (2018).
46. R. Chouaib *et al.*, A dual protein-mRNA localization screen reveals compartmentalized translation and widespread co-translational RNA targeting. *Dev. Cell* **54**, 773–791.e775 (2020).
47. A. Horani, T. W. Ferkol, S. K. Dutcher, S. L. Brody, Genetics and biology of primary ciliary dyskinesia. *Paediatr. Respir. Rev.* **18**, 18–24 (2016).
48. M. R. Knowles, M. Zariwala, M. Leigh, Primary ciliary dyskinesia. *Clin. Chest Med.* **37**, 449–461 (2016).
49. Y. Kakihara, W. A. Houry, The R2TP complex: Discovery and functions. *Biochim. Biophys. Acta* **1823**, 101–107 (2012).
50. J. Te, L. Jia, J. Rogers, A. Miller, S. D. Hartson, Novel subunits of the mammalian Hsp90 signal transduction chaperone. *J. Proteome Res.* **6**, 1963–1973 (2007).
51. R. Zhao *et al.*, Navigating the chaperone network: An integrative map of physical and genetic interactions mediated by the hsp90 chaperone. *Cell* **120**, 715–727 (2005).
52. S. Jain *et al.*, ATPase-modulated stress granules contain a diverse proteome and substructure. *Cell* **164**, 487–498 (2016).
53. S. Massenet, E. Bertrand, C. Verheggen, Assembly and trafficking of box C/D and H/ACA snoRNPs. *RNA Biol.* **14**, 680–692 (2017).
54. J. M. Fingerhut, Y. M. Yamashita, mRNA localization mediates maturation of cytoplasmic cilia in *Drosophila* spermatogenesis. *J. Cell Biol.* **219**, e202003084 (2020).
55. R. Sarpal *et al.*, *Drosophila* KAP interacts with the kinesin II motor subunit KLP64D to assemble chordotonal sensory cilia, but not sperm tails. *Curr. Biol.* **13**, 1687–1696 (2003).
56. Y. G. Han, B. H. Kwok, M. J. Kernan, Intraflagellar transport is required in *Drosophila* to differentiate sensory cilia but not sperm. *Curr. Biol.* **13**, 1679–1686 (2003).
57. T. Avidor-Reiss, M. R. Leroux, Shared and distinct mechanisms of compartmentalized and cytosolic ciliogenesis. *Curr. Biol.* **25**, R1143–R1150 (2015).
58. M. Westerfield, The Zebrafish Book: A Guide for The Laboratory Use of Zebrafish (Danio rerio) (University of Oregon Press, ed. 4, 2000).
59. J. He, D. Mo, J. Chen, L. Luo, Combined whole-mount fluorescence in situ hybridization and antibody staining in zebrafish embryos and larvae. *Nat. Protoc.* **15**, 3361–3379 (2020).
60. S. V. Costes *et al.*, Automatic and quantitative measurement of protein-protein colocalization in live cells. *Biophys. J.* **86**, 3993–4003 (2004).
61. S. Yuan, Z. Sun, Microinjection of mRNA and morpholino antisense oligonucleotides in zebrafish embryos. *J. Vis. Exp.* **27**, 1113 (2009), 10.3791/1113.
62. J. Schindelin *et al.*, Fiji: An open-source platform for biological-image analysis. *Nat. Methods* **9**, 676–682 (2012).
63. M. Arzt *et al.*, LABKIT: Labeling and segmentation toolkit for big image data. *Front. Comput. Sci.* **4**, 777728 (2022).
64. X. Han *et al.*, Protocol to extract actively translated mRNAs from mouse hypothalamus by translating ribosome affinity purification. *STAR Protoc.* **2**, 100589 (2021).
65. Y. Chen, S. Wang, SiyuanWangLab/PNAS2024. GitHub. https://github.com/SiyuanWangLab/PNAS2024. Deposited 18 October 2024.